Ultra-small-sample molecular structure detection using microslot waveguide nuclear spin resonance

Yael Maguire*†, Isaac L. Chuang*, Shuguang Zhang*†‡, and Neil Gershenfeld*

*Center for Bits and Atoms and ‡Center for Biomedical Engineering, NE47-379, Massachusetts Institute of Technology, Cambridge, MA 02139-4307

Communicated by Alexander Rich, Massachusetts Institute of Technology, Cambridge, MA, April 6, 2007 (received for review August 25, 2006)

We here report on the design of a planar microslot waveguide NMR probe with an induction element that can be fabricated at scales from centimeters to nanometers to allow analysis of biomolecules at nano- or picomole quantities, reducing the required amount of materials by several orders of magnitude. This device demonstrates the highest signal-to-noise ratio for a planar detector to date, measured by using the anomeric proton signal from a 15.6-nmol sample of sucrose. This probe had a linewidth of 1.1 Hz for pure water without susceptibility matching. Analysis of 1.57 nmol of ribonuclease-A shows high sensitivity in one- and two-dimensional NMR spectra. Along with reducing required sample volumes, this integrated geometry can be packed in parallel arrays and combined with microfluidic systems. Further development of this device may have broad implications not only for advancing our understanding of many intractable protein structures and their folding, molecular interactions, and dynamic behaviors, but also for high-sensitivity diagnosis of a number of protein conformational diseases.

inductive microslot | miniature probe fabrication | nanomole RNAase-A structural detection | nuclear magnetic resonance scaling | ultra-sensitivity

Nuclear magnetic resonance (NMR) is a powerful analytical tool not only for determining complex biomolecular structures (1–4) but also for monitoring molecular dynamics (5–7). Despite its versatility, NMR protein and large-molecule structural analyses currently require large quantities of protein material at high concentration and purity (8–10), and time-consuming data gathering (11–13). Furthermore, it has been difficult to obtain adequate amounts of proteins with high molecular weight, many protein complexes, and especially membrane proteins for structural analysis because they can form insoluble aggregates (14). We here report design and fabrication of a microdevice that can analyze nanomole quantities of proteins (15–19), and that can be integrated in microfabricated systems.

The ultimate sensitivity limit is a single spin. Single-electron spins have been detected by using mechanical oscillations (20) and by single nuclear spins using optical methods (21, 22). For a volume on the order of $\approx 10^8$ spins, a report of a novel semiconductor detection mechanism shows electronic detection of small quantities of spin 3/2 nuclei at the nanoscale (23). However, all of these techniques require low temperatures. For liquid samples at room temperature, pioneering work on fabrication of solenoids around capillary tubes (16, 24) and microfabrication techniques to create planar coils on semiconductor substrates (1, 25) demonstrates that miniaturization of probes is possible and substantially reduces sample quantity while retaining signal sensitivity (15). Solenoidal microcoils detect nanomole quantities with high sensitivity but have not been successfully fabricated below ≈ 300 μm inner diameter (26), whereas planar coils on semiconductor substrates are scalable but show lower signal sensitivity due to inhomogeneous broadening and path loss.

We here report the fabrication of a new geometry for miniaturizing NMR probes called a microslot that produces high signal-to-noise ratio (SNR) sensitivity and high radio frequency (RF) homogeneity (27). As with other miniaturized probes, a microslot has much shorter tipping times for the same power input and very little radiation damping compared with conventional probes, enabling more complex pulse sequences. Moreover, it is not only easily fabricated at a wide variety of scales, but multiple samples can be measured in parallel by an array. In realizing this design, we demonstrate the fabrication of this device and perform a set of experiments to determine the linewidth of water, measure the device's SNR, perform multiple-quantum measurements on a protein ribonuclease-A, and measure agreement with numerical models.

Results

Theoretical Calculation and Numerical Simulations. A microslot is based on a planar, electromagnetic waveguide called a microstrip (28). A microstrip is a dual-layer, metallic, planar structure used for transporting quasi-transverse electromagnetic mode (TEM) RF signals on dielectric materials such as printed circuit boards, microcircuits, and antennas. A small slot (with largest dimension much smaller than the wavelength, λ, of the electromagnetic wave) is cut out from a conventional substrate, producing a pure series inductance, as shown in Fig. 1. This structure was first analyzed at the beginning of microwave very large scale integration design (VLSI) (29) to understand imperfections in circuit design but had never before been used for spin detection. As analyzed by Hoeffer (30), a slot in a microstrip whose size is smaller than the height of the dielectric produces an increased inductance, ΔL of

$$\Delta L = \frac{\mu_0 \pi}{2} h \left[1 - \frac{Z_0}{Z_0'} \sqrt{\frac{\varepsilon_0}{\varepsilon_0'}} \right]^2, \qquad [1]$$

where h is the height of the dielectric, Z_0 and ε_0 are the impedance and dielectric constants of the microstrip, respectively, and Z_0' and ε' are the impedance and dielectric constants of the microstrip at the microslot. The change in inductance, ΔL, created by the microslot flux, ϕ, is

$$\Delta L = \phi / i = \frac{\int_s B \cdot dA}{i}, \qquad [2]$$

with the current i, and an enclosed surface S. Since Eq. **1** is positive, the overall flux density, B, must increase. By reciprocity, the ability to detect magnetic flux density must also increase. This analysis does not provide information about the distribution of flux density; thus, it needs to be supplemented by numerical modeling. Fig. 1 shows several geometries of a microslot on a

Author contributions: Y.M., I.L.C., S.Z., and N.G. designed research; Y.M. performed research; and Y.M., I.L.C., S.Z., and N.G. wrote the paper.

The authors declare no conflict of interest.

Freely available online through the PNAS open access option.

Abbreviations: RF, radio frequency; SNR, signal-to-noise ratio.

†To whom correspondence may be addressed. E-mail: yael@media.mit.edu or shuguang@mit.edu.

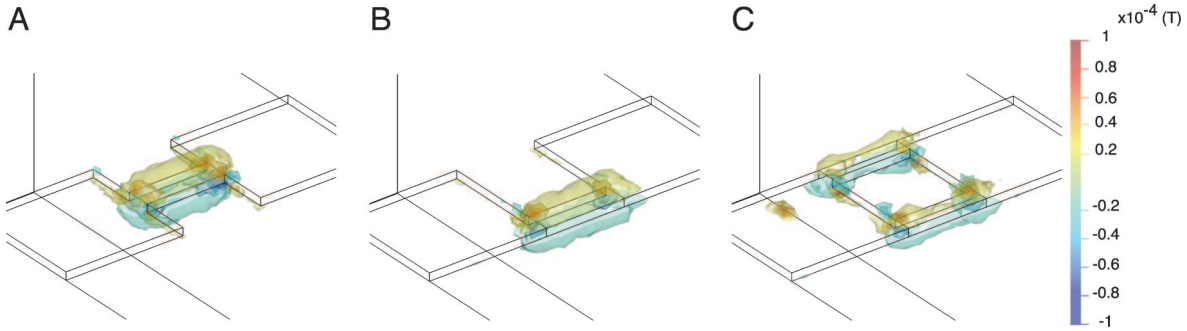

Fig. 1. Different microslot geometries and magnetic flux density patterns around symmetric and asymmetric versions. (*A*) Flux from center. (*B*) Flux from one side. (*C*) Flux from both sides. The magnetic flux density cannot be solved analytically; therefore, a numerical model shows the transverse component (in the long direction of the copper microstrip line) of flux density in each of the cases, showing flux concentration about the microslot in a section on a microstrip line. The unit is tesla.

section of a copper planar waveguide on a dielectric surface. As illustrated, isoshells of the strongest component of the magnetic flux density are concentrated around the slot. Localized to the slot is a highly homogeneous, near-field magnetic flux density that to first order produces no extra electric field component in the vicinity of the sample. These field lines are more homogeneous than those produced by a planar spiral inductor or a simple wire, and we note that the homogeneity of this structure improves at higher frequencies due to current bunching on the sides of the microstrip. By placing a silica capillary tube or drop of sample just above the slot, a strong magnetic flux density will be seen by the nuclear spins of this sample, causing nutation, and the magnetization of the nuclear spins will be converted to a voltage induced in the microslot detector. From the geometrical constraints of the design, an advantage for ionic and/or biological sample detection is that dielectric losses for a microslot probe should be lower than a solenoid. The electric field is confined mostly in the dielectric substrate of the probe, far away from the sample, rather than between windings and in intimate contact with the sample capillary of a solenoid.

Fabrication of the Waveguide Microslot Probe. After theoretical calculation and numerical simulations, we designed and fabricated the waveguide microslot probe itself. The actual waveguide microslot probe is shown in Fig. 2*A*. A macroscopic stripline is impedance-matched with an adiabatic taper to the microfabricated slot (Fig. 2*B*) whose size is on the order of the sample itself (in this case, 200 × 100 μm). The geometry in Fig. 1*C* allowed for rapid design iterations, but it does not have as large a magnetic flux density as the geometry in Fig. 1*A*.

The assembled microslot probe is shown in Fig. 2*A*. The lumped model circuit for the system with matching capacitors is shown in Fig. 2*A*, where the microstrip line and microslot are lumped as a single inductance. The measured circuit quality factor (Q) for this resonant system is 256. This probe circuit design is a single resonance matched network and therefore the microslot network topology is equivalent to a microcoil or conventional probe. Hence, a single microslot inductor can be made multiply resonant in a circuit topology or with multiple single-resonant microslots in proximity with the sample. Due to the small size of the microslot detector, small-shielded gradient coils can be designed on the circuit substrate or around it in air to achieve potentially higher field gradient strengths than can be obtained conventionally.

Sensitivity to Water. To test the microslot probe and characterize its properties, we started with water, which has a single resonance and high SNR. We applied 32 nl of 100% deionized water in a 102-μm fused silica capillary tube. The water sample was suspended 60 μm above the surface of the probe. A single $\pi/2$ rotation pulse (power 0.9 W, duration 6.0 μs) yielded a linewidth of 1.1 Hz and a sensitivity of 1,379/μmol/$\sqrt{\text{Hz}}$, shown in Fig. 3*A Inset*. The base linewidth at 0.55% is not optimized (54 Hz), because we did not apply a susceptibility matching metal bilayer (Fig. 3).

Sensitivity to Sucrose. The next experiment was designed to compare the sensitivity of this probe to the published literature on small sample detection. The convention used to calculate sensitivity independent of the particular magnetic field used in experiment is to measure the SNR of the anomeric proton of sucrose ($C_{12}H_{22}O_{11}$) and scale this value to 600 MHz (26) by a factor $\omega_0^{7/4}$, inductive readout sensitivity scaling (31). Twenty-five nanoliters of sample was prepared at 0.6 M concentration in deionized water (Fig. 4). The sample tube geometry and placement used was the same as in the water experiment above. The measured sensitivity for the microslot probe was 984/μmol/$\sqrt{\text{Hz}}$,

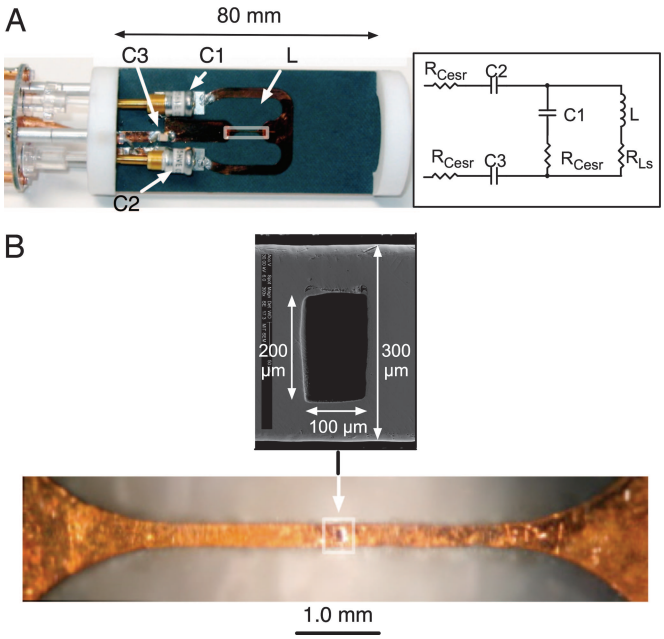

Fig. 2. Designed and fabricated microslot waveguide probe. (*A*) Probe with housing removed. The probe circuit is manufactured on a planar substrate (Rogers 5880), with the detector area denoted by the box outline. (*Inset*) Lumped circuit model of *A*. (*B*) Microslot, fabricated by using a 248-nm excimer laser, just after laser exposure. (*Inset*) Probe after mechanical polishing.

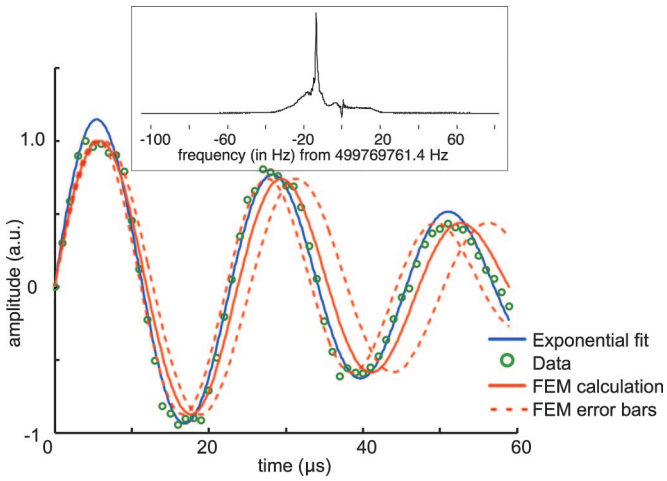

Fig. 3. Nutation plot of the microslot probe with a transmitter power of 1 W. (*Inset*) Sample of 32 nl of 100% deionized H_2O with an SNR of 2,452 and linewidth of 1.1 Hz. The ratio of the peak at an angle of 270° to 90° is 0.97. Overlaid is an exponentially damped sinusoidal fit and a nutation plot predicted by the modeling with circuit parameters measured from the actual probe.

the highest reported for a planar detector (1), with the spectrum Fig. 4. The conventional probe spectrum measured 89.3/μmol/$\sqrt{\text{Hz}}$ in a nonoptimized experiment, and the literature reports 134/μmol/$\sqrt{\text{Hz}}$ (1). Overall, the microslot waveguide is ≈8 times more sensitive and yields ≈8 times narrower lines than other planar probes (1, 25). At this size, the microslot is ≈36% less sensitive than a microcoil used at 500 MHz (26) but can also be scaled to higher sensitivity at smaller sizes. A planar detector can now be used in high-sensitivity applications and scaled to a particular sample size with this integrated design.

Biomolecular Detection. We are very interested in using the microslot waveguide probe to detect common biomolecules including proteins and nucleic acids because NMR is not only widely used for biomolecular detections but also for structural determinations and dynamic studies. The next experimental goal was to test the ability of the microslot probe to detect protein ribonuclease-A (Fig. 5). Samples of 660 μl and 188 nl of the same solution of ribonuclease-A at 8.3 mM were analyzed by using a

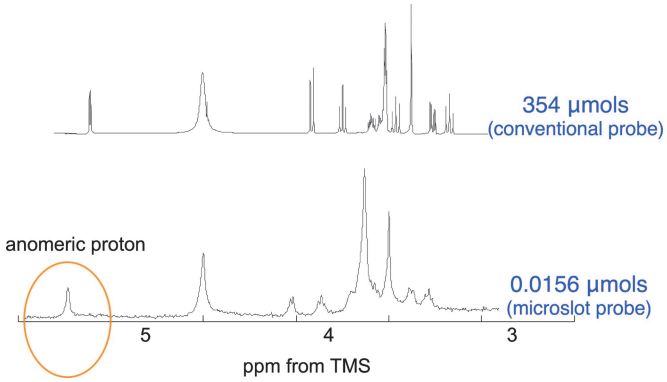

Fig. 4. Sample of 15.6 nmol of sucrose in 100% deionized H_2O acquired in 20 s with the anomeric proton circled (*Lower*), and spectrum from a conventional probe with ≈22,000 times more sample (*Upper*). The shift in spectrum between probes is due to a temperature difference inside the capillary versus a conventional tube. The linewidth appears to be larger than the 1.1 Hz of water due to the overlap of the 54-Hz 90% peak width (≫1 Hz) and due to the lack of a deuterium lock for shimming and sample averaging.

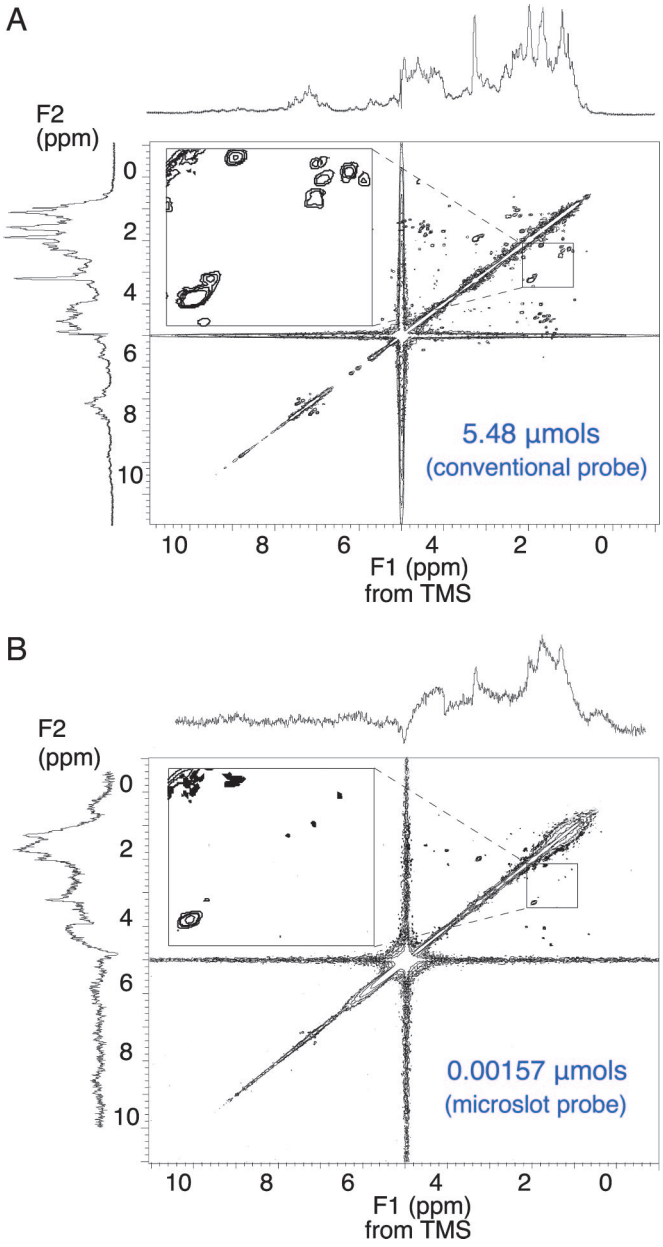

Fig. 5. NMR spectra of protein ribonuclease-A of conventional probe and the microslot probe. (*A*) One- and two-dimensional spectra of 5.48 μmol of ribonuclease-A from a conventional Nalorac 5-mm probe. (*B*) From a microslot probe with 1.57 nmol (≈10^{14} molecules), ≈3,500 times less sample than from the Nalorac probe. The shift in spectra from the probes is due to a difference between the temperature inside the capillary and that inside a conventional tube. The off-diagonal peaks from the microslot appear narrower because the contour algorithm used was normalized to the main diagonal (the off-diagonal satellites are weaker because of inhomogeneous broadening and acquisition time relative to the sample volume).

Nalorac HFX and microslot probe, respectively. A one-dimensional spectrum and a magnitude correlation spectroscopy (COSY) (32) were generated, as shown in Fig. 5. Using the Nalorac probe and larger sample, the COSY was gathered in 12 h, whereas the corresponding data were gathered in 24 h when using the microslot probe. With ≈3,500 times less sample in the capillary of the microslot compared with the traditional probe, we are able to observe off-diagonal structure of the protein in two dimensions. Off-diagonal peak information is observed

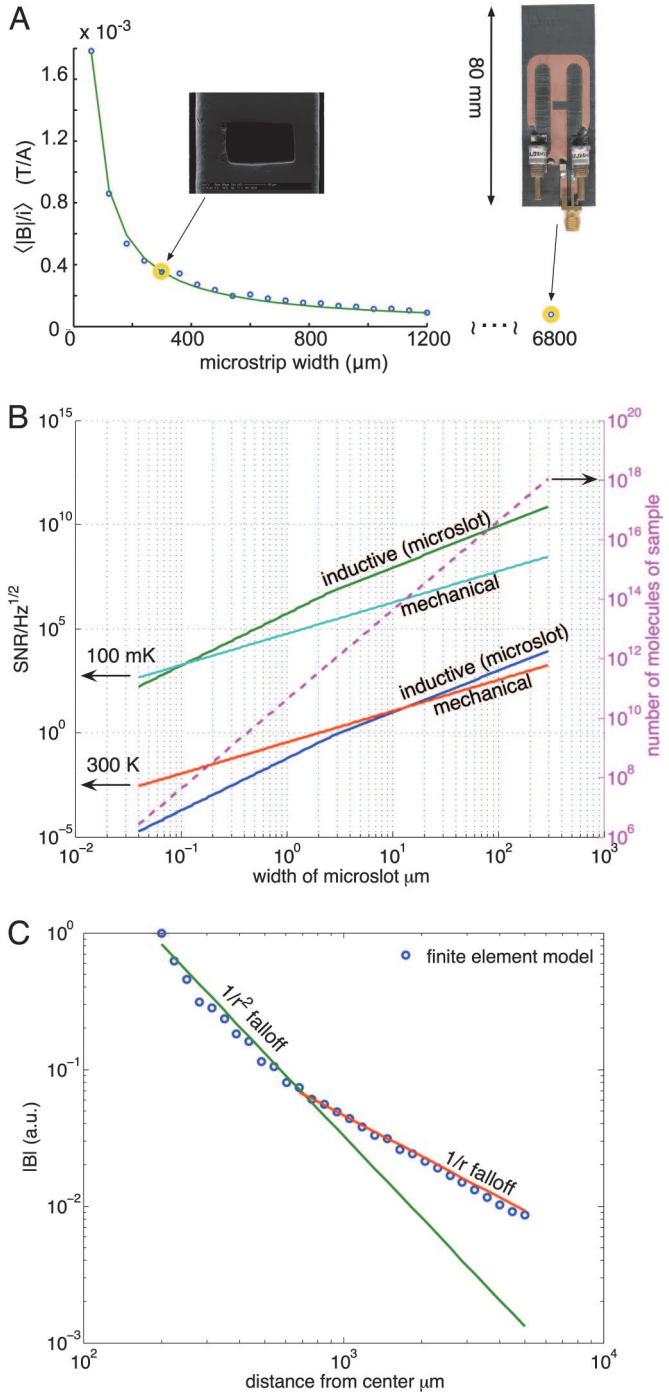

Fig. 6. Scaling and packing properties of the microslot probe. (*A*) Scaling curve of sensitivity versus microslot size calculated by a parameterized finite element model from 60 μm to 6.9 mm. The curve shows a $1/r$ behavior, and data from a 300-μm microslot probe and a 6.9-mm microslot probe (using geometry type B from Fig. 1) show strong agreement with the model. (*B*) Scaling plots of SNR/$\sqrt{\text{Hz}}$ for inductive and mechanical nuclear spin detection at room temperature and 100 mK. The microslot room temperature curve was also calibrated by using real data as in *A*. For a wide span of fabrication scales at low temperature, an inductive microslot should have higher sensitivity than mechanical detection, while preserving chemical shift information. (*C*) Field decay of the microslot detector showing an inductive falloff for the detector, allowing high packing density. The detector size is $d = 297$ μm. At $10d$ from the center of the detector, the field magnitude is at 0.013 of the peak value.

intersecting all areas of the one-dimensional data on both sides of the water peak. It is expected that missing cross-peaks from inhomogeneous broadening can be recovered by a permeability-matched metallization on the surface of the microstripline, a technique used in the design of conventional probes. Given the sensitivity results for sucrose, it would take >1,000 h for a conventional 5-mm probe to collect from this sample the spectra shown in Fig. 5 with equivalent SNR to that obtained by the microslot in just under 24 h.

RF Homogeneity. The final experimental objective was to measure the RF homogeneity of the probe to understand the scaling properties of the microslot and compare this to numerical modeling. A nutation experiment was conducted in which the width of a single pulse was varied as a function of time at a power of 0.9 W. A plot of this experiment is shown in Fig. 3, with a fit from a finite element calculation. The only measured parameter required for the model was the current through the microslot. Network parameters for the circuit model were measured on a network analyzer, and the current was calculated given the input power. From this analysis, we see strong agreement with experiment and the numerical model for the mean RF magnetic field of the probe, B_1 (1). A second probe built for traditional 5-mm sample tubes also had strong agreement with numerical modeling shown in Fig. 6*A*, as described in the next section.

Discussion

A Full Scaling Calculation. With experimental validation of the model for these probes, a full scaling calculation was made from 60 μm to 6.8 mm, as shown in Fig. 6*A*. From this figure, we obtain the same $1/r$ scaling relationship that has been analytically determined for microcoils and planar coils (15). As an example, scaling the detector to a 10 μm width should yield a sensitivity of $\approx 3 \times 10^4/\mu\text{mol}/\sqrt{\text{Hz}}$. Below this scale, at ≈ 3 μm, the skin depth is on the order of the structure. At this scale, the area of electron flow in the conductor goes from being approximated as one-dimensional shell current to a fully two-dimensional one. At this transition, the resistive scaling increases by an additional factor of d, reducing sensitivity to a factor of $1/\sqrt{d}$, down to a limit at which quantum effects become significant.

Signal-to-Noise Scaling. The signal-to-noise scaling comparison of mechanical, spin valve, and inductive detection has been studied in depth (33, 34). Spin valve techniques are not considered here because the magnetization of the detector would go into saturation well below typical magnetic fields required for high chemical shift separation and spin polarization for nuclei (35). For the other detection techniques that are insensitive to the static field, the limiting condition for sensitivity is thermal noise in the detector. For mechanical detection, the limitation is Brownian motion of the oscillator, and for inductive detection it is Johnson noise in the resonant circuit. The ratio of SNR for both techniques is

$$\text{SNR}_{\text{mech}}/\text{SNR}_{\text{ind}} = \frac{\kappa_{\text{mech}}}{\kappa_{\text{ind}}} \frac{M_{\text{d}}}{\omega_0} \sqrt{\frac{\alpha}{R}}, \qquad [3]$$

where $\kappa_{\text{mech,ind}}$ are shape factors for each solution, M_{d} is the magnetization of the mechanical detector, and α and R are the respective dissipation factors (33). In Fig. 6, the sensitivity of the microslot and a mechanical detector is compared with decreasing size, at room and low temperature. The room temperature microslot curve is calibrated with data obtained from the 300-μm-microslot experiments. At 800 MHz, a microslot width of 13.4 μm, and room temperature, this plot verifies that a mechanical detector should be more sensitive than an inductive microslot at the expense of chemical shift information. This is

because of the scaling of the noise in a mechanical detector, $\alpha = m\omega/Q$, which is largely independent of temperature (36), yields high Q values at room temperature, whereas resistive losses have a linear dependence on temperature. However, an inductive detector has higher order ($T^{1/2}$) noise scaling versus temperature. The surprising implication of this is that at low temperature (for example, 100 mK), an inductive microslot will have higher SNR than mechanical detection down to ≈100 nm as shown in Fig. 6. Biological samples will be frozen at this temperature, requiring nonstandard techniques or thermomechanical assemblies, but for low-temperature physics experiments (20), a microslot could be a useful nuclear spin detector.

Potential Applications. A final consideration for applications is the packing density of this detector. With the simple design of the microslot, planar arrays of microslots can easily be fabricated and used for parallel measurements. Multiple microslots could be used to simultaneously measure different time slices of an experiment, parallel measurements could be made on multiple samples, and an array of detectors provides an alternative to gradient-based imaging. A concern with any magnetic probe for this purpose is the ability to minimize mutual interaction among sensors. From Fig. 6*C*, the field strength in the substrate plane perpendicular to the 297-μm probe was calculated from a finite element model. This shows that at a distance far from the length of the structure ($\gg$297 μm), we see the field is not falling off as a dipole radiator but has an inductive falloff ($1/r^2$) for a significant distance. By reciprocity, this makes the microslot a favorable structure for packing. As an example, a design of 50-μm-diameter microslots separated by a distance where the field strength of a nearest neighbor is ≈1/100 the peak field strength value would yield 100 sensors within a 5 mm × 5 mm square, the typical area of an NMR sample tube.

Advantages of Microslot Waveguide Probe. Our planar microslot waveguide geometry is one of the smallest and simplest NMR probe designs, is scalable to submicrometer feature sizes, and can be fabricated in parallel arrays for combinatorial measurements. The two-dimensional spectrum of ribonuclease-A in Fig. 5*B* was measured on ≈10^{14} molecules, comparable to the number of molecules contained in a spot in a two-dimensional gel (37, 38) and matching at room temperature the result achievable with a cryogenically cooled probe. The use of microslots may provide enough information to determine structural information from a single protein spot, and if parallelized, many spots simultaneously. Beyond reducing sample volumes, the integrated planar fabrication of the microslot probe can be combined with microscopy on living systems, with other spectroscopies such as GC-MS and HPLC, and with other microstructures including microfluidic sample handling (39, 40) and electronic instrumentation, and can be used for other magnetic probes including electron polarization resonance (EPR), microscopic field mapping, and microelectronic signal detection.

Impact in Structural Biology, Structural Genomics, and Other Fields. With several orders of magnitude sample reduction for structural detection and determination, the microslot waveguide NMR probe could have broad implications not only in speeding up biological research on structural genomics, high-throughput protein structural determination, the study of protein folding, and protein–protein and protein–ligand interactions and their dynamic behaviors, but also in developing applications of NMR in pharmaceutics and medical diagnoses.

Materials and Methods

NMR Experiments. NMR Experiments were carried out by using an 11.7-T Oxford Instruments magnet, a four-channel Varian UNITYINOVA spectrometer, and a custom-built probe containing the microslot waveguide. The probe circuit board was chemically etched with conventional circuit board techniques by Cirexx. The active element of the probe was microfabricated from 60-μm-thick copper on Rogers 5880, a glass-reinforced PFTE substrate that has very low tangent loss at radio frequencies ($\delta = 0.0004$ at 1.0 GHz). The main pattern shown in Fig. 2*A* was made by traditional chemical etching on the circuit board material. The microfabricated slot was made on a Resonetics 248-nm excimer laser micromachining-centre with a fluence of ≈21 J/cm^2. This system was chosen over traditional microfabrication techniques because of the ease with which high-aspect-ratio patterns in 60 μm of copper can be created in seconds without a photo-mask.

Polishing the Microslot. Because of its high heat capacity, some copper remelted on the surface of the structure after micromachining. In addition, the original surface finish of the copper had large features that could cause B_0 inhomogeneity problems with the sample close to the surface. To remove these imperfections, stages of micropolish solutions from Buehler were used. The surfaces were initially rinsed with distilled water and isopropanol. Then, a Buehler 2 7/8-inch Texmet 1000 polishing disk was dabbed with MetaDi 9-μm-diamond paste and soaked with MetaDi solution (Buehler). To preserve the edges of the stripline, the wiping motion was confined to the axis of the microstrip. This motion was performed for ≈2–5 min. The surface was washed in water and isopropanol, and viewed under an optical microscope to observe the progress. This sequence was repeated several times until a consistent finish was seen. This overall process was then repeated with a 3-μm-diamond paste followed by a 1-μm-diamond paste. Because the grain size was now small compared with feature size, polishing was done in a circular manner to obtain an isotropic finish.

Sample Preparation and Experiment Setup. One hundred percent deionized H_2O was used in microcapillary tubing from Polymicro Technologies. This 100-μm-i.d., 165-μm-o.d. tubing is coated with a thin layer of polyimide. It was then cut to a length of ≈6 mm by passing a hobby knife lightly over the surface of the capillary. Then, both ends of the tube were held under tension and pulled apart. This achieved a very clean cut on both ends. The capillary was taped down with Kapton tape to a flat surface and run under a high-pressure stream of tap water to remove all debris from the inside. Using a spray bottle of deionized water, the capillary was rinsed with high-velocity water to force the tap water out. The capillary was then sprayed with compressed air and allowed to dry while it was monitored under a microscope. The washing/drying process was repeated two to three times to remove any debris, with a final rinse and dry in isopropanol. Once dry, a small drop of deionized water was placed on one end of the tube and immediately sucked in via capillary forces. To prevent rapid evaporation, the capillary tube was sealed by dipping its ends into a tacky wax from McMaster-Carr (part no. 1129K14) and then wiping away any excess with isopropanol. For the sucrose experiment, a 0.59 M solution was created, and then a 3.38-mm-long sample was created by means of capillary action. An experiment was performed with 16 scans and an acquisition time of 1.25 s and line-broadening of 1.3 Hz. For the ribonuclease-A experiment, 90.3 mg of sample was dissolved in 700 μl of solution containing 630 μl of 99% D_2O buffer and a 1× buffer of 70 μl of 1,000 mM NaCl and 500 mM NaH_2PO_4. Six hundred sixty microliters of this solution was placed in a standard precision 5-mm 528-PP-8 tube from Wilmad. For the one-dimensional experiments, a standard CW water suppression was applied, and data were collected for 22 s with a spectral width of 6 kHz and acquisition time of 2.0 s. The two-dimensional experiment had the same spectral width in both dimensions (6,024 Hz), an acquisition time of 0.170 s per scan, eight scans,

with 10.0 s of water presaturation delay, 512 T_1 slices for a total of 11.65 h. The tip angle was $\pi/2$ (11.1 μs at the maximum power settings of the console), no apodization was applied, line-broadening was 0.6 and 0.32 Hz, the sinebell constant was 0.085 and 0.021, and the Gaussian time constant was 0.20 and 1.0, respectively, for the directly and indirectly detected dimension. For the microslot protein experiments, the sample was transferred from the 5-mm tube into a 248-μm-i.d. (356 μm o.d.) capillary tube filled 3.89 mm in length. The ends of the 8-mm total tube length were sealed with a fast dry epoxy with an air buffer on both sides of the sample. The one-dimensional experiment had the same spectral width and acquisition time with 16 scans for a total acquisition time of 11.2 min (20 s of sample cooling time was added to each run). The two-dimensional experiment also had the same spectral width (6,024 Hz) and acquisition time (0.170 s per scan, 512 T_1 slices, eight scans, 10.0 s of water presaturation delay, and 10.0 s of recycle delay) parameters with a total acquisition time of 23.28 h. The tip angle was $\pi/2$ (8.75 μs at 11 dB lower than the maximum power setting of the console), no apodization was applied, line-broadening was 0.6 and 0.32 Hz, the sinebell constant was 0.085 and 0.021, and the Gaussian time constant was 0.20 and 1.0, respectively, for the directly and indirectly detected dimension.

We thank Peter Carr for help on NMR sample preparation and data analysis; K. Brown, R. Clark, D. Cory, J. Difrancesco, and K. Mehr for technical assistance; and T. de Sweit, T. Barbara, Andreas Mershin, and Sotirios Koutsopoulos for discussions. This work was supported by the Massachusetts Institute of Technology Center for Bits and Atoms through National Science Foundation Grant CCR0122419.

1. Massin C, Vincent F, Homsy A, Ehrmann K, Boero G, Besse PA, Daridon A, Verpoorte E, de Rooij NF, Popovic RS (2003) *J Magn Reson* 164:242–255.
2. Fiaux J, Bertelsen E, Horwich A, Wutrich K (2002) *Nature* 418:207–211.
3. Fernandez C, Wuthrich K (2003) *FEBS Lett* 555:144–150.
4. Wuthrich K (2003) *J Biomol NMR* 27:13–39.
5. Radford S, Woolfson D, Martin S, Lowe G, Dobson CM (1991) *Biochem J* 273:211–217.
6. Nowak U, Li X, Teuten A, Smith R, Dobson CM (1993) *Biochemistry* 32:298–309.
7. Chamberlain A, Receveur V, Spencer A, Redfield C, Dobson CM (2001) *Protein Sci* 10:2525–2530.
8. Yokoyama S (2003) *Curr Opin Chem Biol* 7:39–43.
9. Montelione G, Zheng D, Huang Y, Gunsalus K, Szyperski T (2000) *Nat Struct Biol* 7(Suppl):982–985.
10. Rehm T, Huber R, Holak T (2002) *Structure (London)* 10:1613–1618.
11. Cavanaugh J, Fairbrother WJ, Palmer AG, III, Skelton NJ (1996) *Protein NMR Spectroscopy: Principles and Practice* (Academic, New York).
12. Krishna NR, Berliner LJ, eds (2003) *Protein NMR for the Millennium*, Biological Magnetic Resonance (Kluwer Academic, Dordrecht, The Netherlands), Vol 20.
13. Downing AK, ed (2004) *Methods Mol Biol (Totowa, NJ)* 278.
14. Dobson C (2003) *Nature* 426:884–890.
15. Peck TL, Magin RL, Lauterbur PC (1995) *J Magn Reson Ser B* 108:114–124.
16. Olson DL, Peck TL, Webb AG, Magin RL, Sweedler JV (1995) *Science* 270:1967–1970.
17. Peti W, Norcross J, Eldrige G, O'Neil-Johnson M (2004) *J Am Chem Soc* 126:5873–5878.
18. Brey WW, Edison AS, Nast RE, Rocca JR, Saha S, Withers RS (2006) *J Magn Reson* 179:290–293.
19. Li Y, Webb AG, Saha S, Brey WW, Zachariah C, Edison AS (2006) *Magn Reson Chem* 44:255–262.
20. Rugar D, Budakian R, Mamin H, Chui B (2004) *Nature* 430:329–332.
21. Salis G, Fuchs DT, Kikkawa JM, Awschalom DD, Ohno Y, Ohno H (2001) *Phys Rev Lett* 86:2677–2680.
22. Brouwer A, Kohler J, Groenen E, Schmidt J (1996) *J Chem Phys* 105:2212–2222.
23. Yusa G, Muraki K, Takashina K, Hashimoto K, Hirayama Y (2005) *Nature* 434:1001–1005.
24. Rogers JA, Jackman RJ, Whitesides GM, Olson DL, Sweedler JV (1997) *Appl Phys Lett* 70:2464–2468.
25. Stocker J, Peck T, Webb A, Magin R (1997) *IEEE Trans Biomed Eng* 44:1122–1126.
26. Lacey ME, Subramanian R, Olsen DL, Webb AG, Sweedler JV (1999) *Chem Rev* 99:3133–3152.
27. Maguire Y (2004) PhD thesis (Massachusetts Institute of Technology, Cambridge, MA).
28. Pozar DM (1990) *Microwave Engineering* (Addison–Wesley, Reading, MA).
29. Jackson R, Pozar D (1985) *IEEE Trans Microwave Theory Tech* 33:1036–1042.
30. Hoefer WJR (1977) *IEEE Trans Microwave Theory Tech* 25:822–824.
31. Hoult DI, Richards R (1976) *J Magn Reson* 24:71–85.
32. Ernst RR, Bodenhausen G, Wokaun A (1987) *Principles of Nuclear Magnetic Resonance in One and Two Dimensions* (Clarendon, Oxford, UK).
33. Leskowitz GM, Madsen LA, Weitekamp DP (1998) *Solid State Nucl Magn Reson* 11:73–86.
34. Baibich MN, Broto JM, Fert A, Nguyen Van Dau F, Petroff F, Etienne P, Creuzet G, Friederich A, Chazelas J (1998) *Phys Rev Lett* 61:2472–2475.
35. Mancoff FB, Dunn JH, Clemens B, White R (2000) *Appl Phys Lett* 77:1879–1881.
36. Yasamura KY, Stowe TD, Chow EM, Pfafman T, Kenny TW, Stipe BC, Rugar D (2000) *J Microelectromech Syst* 9:117–125.
37. GE Healthcare (2005) *2-D Electrophoresis: Principles and Methods* (GE Healthcare Amersham Biosciences, Little Chalfont, Buckinghamshire, UK).
38. Simpson RJ, ed (2002) *Proteins and Proteomics: A Laboratory Manual* (Cold Spring Harbor Lab Press, Cold Spring Harbor, NY).
39. Gravensen P, Branebjerg J, Jensen O (1993) *J Micromech Microeng* 3:168–182.
40. Prakash M, Gershenfeld N (2007) *Science* 315:832–835.